







Mantle-to-crust metal transfer by nanomelts

Erwin Schettino ^{1,2✉}, José María González-Jiménez¹, Claudio Marchesi^{1,2}, Francesco Palozza ^{3,4},
Idael F. Blanco-Quintero ⁵, Fernando Gervilla^{1,2}, Roberto Braga ³, Carlos J. Garrido ¹ & Marco Fiorentini ⁴

The transfer of chalcophile metals across the continental lithosphere has been traditionally modeled based on their chemical equilibrium partitioning in sulfide liquids and silicate magmas. Here, we report a suite of Ni-Fe-Cu sulfide droplets across a trans-lithospheric magmatic network linking the subcontinental lithospheric mantle to the overlying continental crust. Petrographic characteristics and numerical calculations both support that the sulfide droplets were mechanically scavenged from the mantle source during partial melting and transported upwards by alkaline magmas rising through the continental lithosphere. Nanoscale investigation by high-resolution transmission electron microscopy (HR-TEM) documents the presence of galena (PbS) nanoinclusions within the sulfide droplets that are involved in the mantle-to-crust magma route. The galena nanoinclusions show a range of microstructural features that are inconsistent with a derivation of PbS by exsolution from the solid products of the Ni-Fe-Cu sulfide liquid. It is argued that galena nanoinclusions crystallized from a precursor Pb(-Cu)-rich nanomelt, which was originally immiscible within the sulfide liquid even at Pb concentrations largely below those required for attaining galena saturation. We suggest that evidence of immiscibility between metal-rich nanomelts and sulfide liquids during magma transport would disrupt the classical way by which metal flux and ore genesis are interpreted, hinting for mechanical transfer of nanophases as a key mechanism for sourcing the amounts of mantle-derived metals that can be concentrated in the crust.

¹Instituto Andaluz de Ciencias de la Tierra, Consejo Superior de Investigaciones Científicas-Universidad de Granada, Avenida de las Palmeras 4, 18100 Armilla, Spain. ²Departamento de Mineralogía y Petrología, Universidad de Granada, Avenida Fuentenueva s/n, 18002 Granada, Spain. ³Department of Biological, Geological and Environmental Sciences, Bologna University, Piazza di Porta S. Donato 1, 40126 Bologna, Italy. ⁴Centre for Exploration Targeting, School of Earth Sciences, ARC Centre of Excellence for Core to Crust Fluid Systems, University of Western Australia, Perth, WA 6009, Australia. ⁵Departamento de Ciencias de la Tierra y del Medio Ambiente, Facultad de Ciencias, Universidad de Alicante, 03690 Alicante, Spain. ✉email: eschettino@correo.ugr.es

Growing demand for high-tech critical commodities to fuel the global sustainable energy transition¹ has recently fostered attention on how base (e.g., nickel, zinc, copper, and lead), precious (e.g., platinum-group elements, gold, and silver) and semi-metals (e.g., tellurium, arsenic, bismuth, and antimony) are concentrated into specific domains of the Earth's crust (i.e., ore deposit formation). The most up-to-date metallogenic models employed for mineral exploration targeting regard ore deposits as local manifestations of large-scale geological processes that optimally align to maximize the flux and storage of metals from background levels in a source region to economic abundances in the accessible crust^{2,3}. The flux of metals is especially enhanced along the tectonically active, trans-lithospheric boundaries that suture the architecture of the continental lithosphere^{4–6}. These regions usually host a great variety of magmatic and/or hydrothermal ore deposits that are fed by magmas extracting metals from fertile volumes of the subcontinental lithospheric mantle (SCLM)^{6–11}. However, the mechanisms controlling the mantle-to-crust metal transfer and the geological repositories that drive the metallogenic storage in ore-productive domains of the continental lithosphere, are still under vigorous debate^{12–14}.

The flux of precious and semi-metals through the continental lithosphere is thought to be governed by their relative solubility within ascending silicate magmas and/or immiscible droplets of Fe-Ni-Cu sulfide liquid^{12,13,15,16}, which collect most of the budget of chalcophile (i.e., sulfide-loving) metals by chemical equilibrium partitioning¹⁷. Then, the upwards ascent of metal-endowed magmas may eventually feed the transfer of metals and sulfur into mineralizing hydrothermal fluids and brines^{13,18} that exsolve at shallow crustal depths^{14,19–21}. This general picture has been challenged by an increasing number of mineralogical studies reporting the occurrence of metal-rich, insoluble nanoparticles controlling a large fraction of the metallogenic inventory of mantle rocks^{11,22,23}, mantle-derived magmas^{24–26}, and hydrothermal ore-forming fluids^{14,27–29}. The entrapment and mechanical transport of these metal-rich nanoparticles could provide an efficient mechanism for upgrading the metal concentrations of sulfide melts^{11,25} and hydrothermal solutions²⁷. These key findings question the reliability of solubility models and chemical equilibrium partitioning in predicting the behavior of metals in both magmatic and hydrothermal ore systems^{30,31}. Nevertheless, the origin of metal-rich nanoparticles in mantle rocks, as well as their fate during transport upwards through the crust, are still contentious questions. Experimental work shows that precious and semi-metals in magmas tend to self-organize into insoluble nanoclusters and/or nanomelts, even prior to attaining saturation contents in sulfide liquids^{32,33}. However, the geological record still lacks direct evidence of lithospheric-scale metal transport via immiscible metal-rich nanomelts, with little knowledge of their impact on the mobility and storage of metals in ore-productive domains of the continental lithosphere.

To address this knowledge gap, we investigated rocks from the Neogene Volcanic Province of the Eastern Betics (southeastern Spain), which hosts a wide range of magmatic-hydrothermal ores associated with subduction-related magmatism in the western Mediterranean. This volcanic province includes calc-alkaline to alkaline magmas³⁴, which are genetically associated with epithermal Au and Pb-Zn-Cu-(Ag) mineralization at ~9–11 Ma in the Roadalquilar-Carboneras and Mazarrón-La Unión districts, respectively^{35,36} (Fig. 1A). The last eruptive stages of alkaline basalt magmatism (Tallante volcanic field, 2.93–2.29 Ma; Fig. 1A) brought up to the surface abundant mantle xenoliths representative of the underlying SCLM, which was inferred to have originally fed the ore-productive volcanism in the region¹¹. Moreover, alkaline magmatism in the region produced lamproite dykes, which extruded at ~9.3–7.1 Ma³⁷ (e.g., Fortuna volcanic

field, Fig. 1A) and were sourced by partial melting of the subduction-metasomatized SCLM sampled by the Tallante mantle xenoliths^{38–40}. Therefore, the Neogene Volcanic Province of SE Spain is an excellent natural laboratory for documenting the transfer mechanisms that controlled the flux of metals from the SCLM to magmatic-hydrothermal ores in the upper crust across a trans-lithospheric plumbing network.

Here, we discuss the mechanisms accounting for mantle-to-crust metal transfer by describing the nature of Pb-rich nanoparticles preserved in metasomatized mantle xenoliths¹¹ (Tallante volcanic field) and their inferred magmatic outputs^{38,39} (Fortuna lamproite dykes). Our observations provide snapshots of metal transport in a trans-lithospheric continuum and document how mechanical entrapment of metal-rich nanomelts immiscible in sulfide liquid may play a key role in regulating the metal endowment through an ore-productive sector of continental lithosphere.

Results

Galena nanoinclusions in Tallante mantle xenoliths. Pb-rich nanoinclusions were detected within a sulfide droplet hosted in metasomatic clinopyroxene from Tallante peridotite xenoliths (Fig. 1B). A detailed description of the petrogenesis of Tallante peridotite xenoliths is provided in the Supplementary Note 1. The nanoparticle-bearing sulfide is a ~30 μm size spherical droplet and consists of pentlandite [(Ni,Fe)₉S₈] intergrown with lesser amounts of chalcopyrite [CuFeS₂] and bornite [Cu₅FeS₄] (Fig. 2A). Analogous pyroxene-hosted sulfides in the Tallante mantle xenoliths were interpreted to have precipitated from immiscible droplets of Ni-Fe-Cu sulfide liquid, which were carried by asthenosphere-derived silicate magmas percolating through the shallow SCLM in the Miocene¹¹. The selected sulfide droplet hosts several high atomic weight (bright colors in the BSE images) euhedral nanoinclusions (Fig. 2A) characterized by Pb, S, and minor Cu peaks in the energy dispersive X-ray spectra (EDS; Supplementary Fig. 1). Two Pb-rich nanoinclusions were sampled by focused-ion beam scanning electron microscope (FIB-SEM) and examined under high-resolution transmission electron microscopy (HR-TEM).

The FIB section extracted from the inner part of the sulfide droplet contains a Pb(-Cu)-rich idiomorphic nanoinclusion (~100 nm; Fig. 2B), which is randomly oriented within a homogeneous Ni-Fe pentlandite matrix (Supplementary Fig. 6). The corresponding selected area electron diffraction (SAED) patterns of the Pb(-Cu)-rich nanoinclusion yield d-spacings of 1.75 and 2.99 Å (Table 1) matching with the (3 1 1) and (2 0 0) planes of galena [PbS], respectively. The small proportions of Cu relative to Pb in this mineral, as determined by the corresponding peaks in the EDS spectra (Supplementary Fig. 1), point out that minor amounts of Cu could be effectively accommodated into the crystal lattice of galena in solid solution^{41,42}. The galena nanoinclusion displays well-defined crystal faces and polygonal grain boundaries (Fig. 2C). Moreover, the HR-TEM imaging highlights that the galena nanoinclusion, identified by (2 2 0) and (2 0 0) planes (2.10 and 2.97 Å d-spacings, respectively), exhibits a distinct lattice orientation compared to the surrounding pentlandite, identified by (3 1 1) plane (3.08 Å d-spacings), as shown in Fig. 2D. The TEM-EDS elemental mapping of the FIB section also reveals the presence of a Fe-oxide euhedral inclusion (~500 nm, Supplementary Fig. 6). The fast Fourier diffraction patterns calculated from high-resolution TEM images of the Fe-oxide yield d-spacings of 2.95 and 5.13 Å, which match with the (2 2 0) plane and double d-spacing of (3 1 1) plane of magnetite, respectively (Table 1). The HR-TEM imaging indicates that the magnetite inclusion shares a common crystallographic orientation with the surrounding pentlandite matrix (Supplementary Fig. 7).

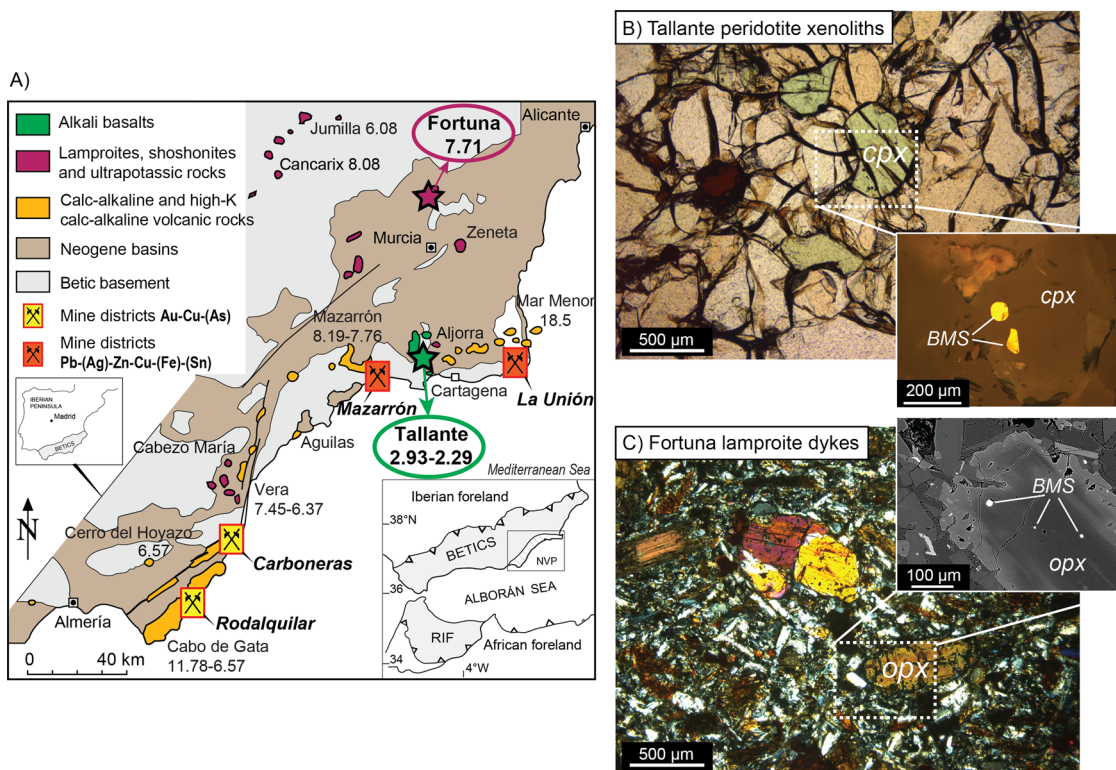


Fig. 1 Geological setting and petrographic textures of peridotite xenoliths (Tallante volcanic field) and lamproite dykes (Fortunal volcanic field) from the Neogene Volcanic Province of southeast Spain. A Geological map of the Neogene Volcanic Province of southeast Spain (modified after⁷⁴), showing the location of the volcanic outcrops and of various magmatic-hydrothermal ore deposits. Geochronological data in million years (Ma) of volcanic suites are from ref. ³⁴. **B** Photomicrographs and backscatter electron images of the studied clinopyroxene-hosted sulfides from the Tallante peridotite xenoliths. **C** Photomicrographs and backscatter electron images of the studied orthopyroxene-hosted sulfides from the Fortuna lamproite dykes. Mineral abbreviations are cpx clinopyroxene, opx orthopyroxene, and BMS base-metal sulfides.

The FIB section extracted from the margin of the Tallante sulfide crosscuts a $\sim 1 \mu\text{m}$ size Pb-rich idiomorphic grain, which is located along the outer margin of the chalcopyrite portion of the sulfide droplet (Fig. 2A, E). The Pb-rich nanoinclusion yields single-crystal diffraction patterns of 1.79 \AA , which is consistent with the (3 1 1) plane of galena (Table 1). The TEM-EDS elemental mapping shows that the galena inclusion is rimmed by a subspherical Cu-rich halo (Fig. 2E), which yields single-crystal diffraction patterns of 3.38 \AA matching with the (1 0 0) plane of digenite $[\text{Cu}_9\text{S}_5]$. The HR-TEM imaging reveals that the galena inclusion, identified by the (1 1 1) plane (3.42 \AA d-spacing), shares a common crystallographic orientation with the adjacent digenite halo, identified by (3 2 2) plane (3.05 \AA d-spacing), as shown in Fig. 2G.

Galena nanoinclusions in Fortuna lamproite dykes. Pb-rich nanoinclusions are also observed within sulfide droplets in the Fortuna lamproite dykes. Further details into the petrogenesis of Fortuna lamproite rocks are provided in Supplementary Note 1. These nanoparticle-bearing sulfides are $\sim 10 \mu\text{m}$ size rounded droplets included within the core ($\text{Mg}\# = 94.5\text{--}87.3$) of prismatic orthopyroxene phenocrysts (Fig. 1C). The sulfides droplets consist of pentlandite and chalcopyrite intergrowths (Fig. 3A), with rare amounts of pyrrhotite, and are commonly associated with fluid inclusions and/or silicate melt inclusions (Fig. 3A and Supplementary Figs 2–5). The sulfide droplets in the Fortuna lamproites were interpreted to have precipitated from immiscible droplets of Ni-Fe-Cu sulfide liquid⁴³, which were trapped within growing orthopyroxene as the lamproite magmas ascended from the mantle source to crustal magma chambers⁴⁴. Abundant Pb-

rich inclusions ($0.1\text{--}1 \mu\text{m}$ in size), showing minor or negligible amounts of Cu in their EDS spectra (Supplementary Figs. 2–5), were detected along the edge surface of these sulfide droplets (Fig. 3A). A total of four Pb-rich nanoinclusions were sampled by focused-ion beam and subsequently analyzed by HR-TEM.

In all FIB sections, the selected area and single-crystal diffraction patterns of Pb(-Cu)-rich nanoinclusions (Fig. 3B, E) are consistent with single crystals of galena (Table 1). Again, the small proportions of Cu relative to Pb in the corresponding EDS spectra (Supplementary Figs. 2–5) suggest that the galena nanoinclusions accommodated minor amounts of Cu in solid solution^{41,42}. The HR-TEM imaging indicates that galena nanoinclusions are in crystallographic continuity with the surrounding pentlandite matrix (Fig. 3G). However, these galena nanoinclusions show no preferential orientation relative to the subparallel planar intergrowths of pentlandite-chalcopyrite and pyrrhotite in the host sulfide (Fig. 3B), nor crystallographic continuity with the adjacent orthopyroxene phenocryst (Fig. 3D). Moreover, the galena nanoinclusions exhibit semi-circular morphologies, with an outer border that typically adapt along the curvilinear surface of the host sulfide droplets (Fig. 3B, C, E, F).

Discussion

The galena-bearing sulfide droplets in the Tallante mantle xenoliths and the Fortuna lamproite dykes share very similar textural and compositional characteristics. They both consist of $\sim 10\text{--}30 \mu\text{m}$ rounded grains made of pentlandite \pm chalcopyrite intergrowths and host an identical suite of nano-to-micrometer sized mineral inclusions, such as galena (Figs. 2, 3) as well as native gold^{11,23,45}. These observations led us to put forward the hypothesis that the

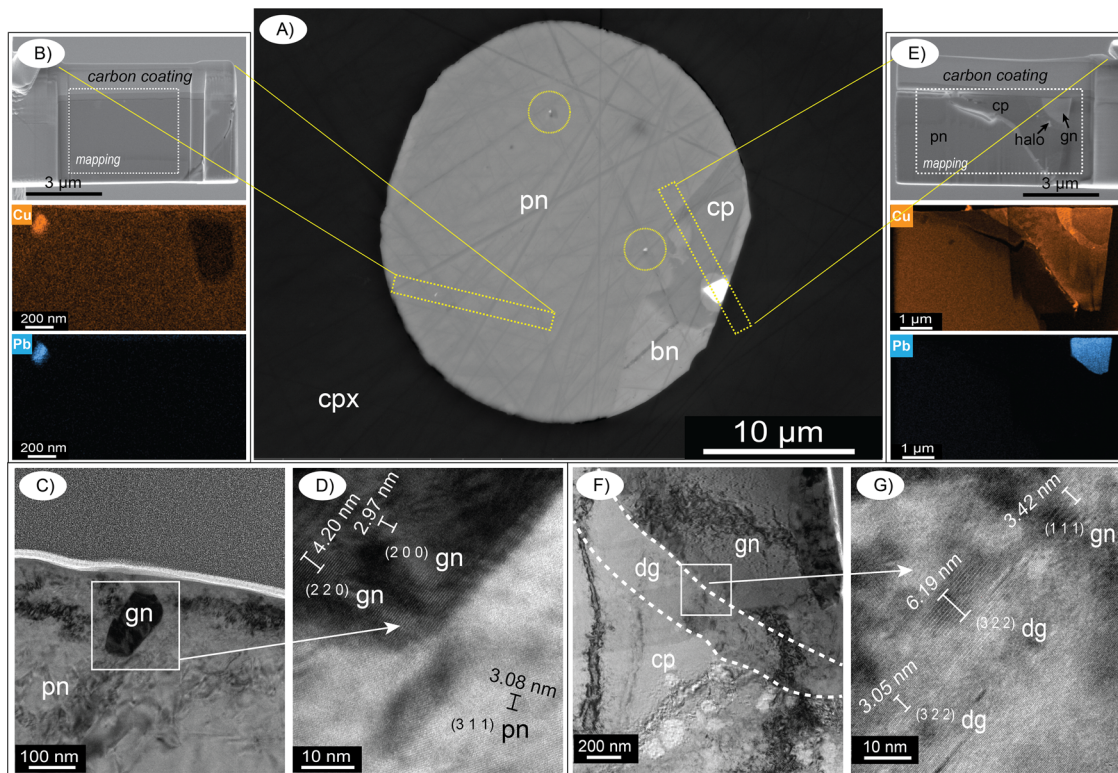


Fig. 2 Sulfide-hosted galena nanoinclusions in Tallante peridotite xenoliths. Backscatter electron image acquired at scanning electron microscope on polished thin section, showing the location of two Pb-rich nanoparticles in the studied sulfide droplet from Tallante peridotite xenoliths (A). Backscatter electron images and EDS elemental maps (Cu, Pb) on the two thin foil focused-ion beam (FIB) sections were analyzed by transmission electron microscopy (TEM) (B, E). Bright-field images in scanning transmission electron microscopy (STEM mode; C, F) and high-resolution TEM images (D, G) of the contact between the galena nanoinclusions and the adjacent sulfide minerals. Estimated measurements (nm) of ten spacings and corresponding lattice parameters are shown for each mineral domain. Mineral abbreviations are cpx clinopyroxene, gn galena, pn pentlandite, cp chalcopyrite, bn bornite, dg digenite.

Table 1 Indexed lattice parameters of identified minerals derived from selected area electron diffraction (SAED) analysis and fast Fourier Transform (FFT) diffraction patterns calculated from high-resolution images (Supplementary Fig. 13).

d-spacings (Å)	pentlandite		chalcopyrite		galena		digenite		magnetite	
	Å	(h k l)	Å	(h k l)	Å	(h k l)	Å	(h k l)	Å	(h k l)
Tallante peridotite xenolith										
3.54	3.50	2 2 0								
3.02	3.08	3 1 1								
2.89	2.85	2 2 2								
3.03			3.04	1 1 2						
1.87			1.87	2 2 0						
3.42					3.42	1 1 1				
2.96					2.99	2 0 0				
2.09					2.10	2 2 0				
1.78					1.79	3 1 1				
3.38							3.38	1 0 0		
3.04							3.05	3 2 2		
2.96									2.95	2 2 0
2.53									2.56	3 1 1
Fortuna lamproite dyke										
5.79	5.79	1 1 1								
3.54	3.55	2 2 0								
3.02	3.01	3 1 1								
2.89	2.87	2 2 2								
1.77	1.80	4 4 0								
3.04			3.07	1 1 2						
1.87			1.88	2 2 0						
3.42					3.42	1 1 1				
2.96					2.96	2 0 0				
2.09					2.06	2 2 0				

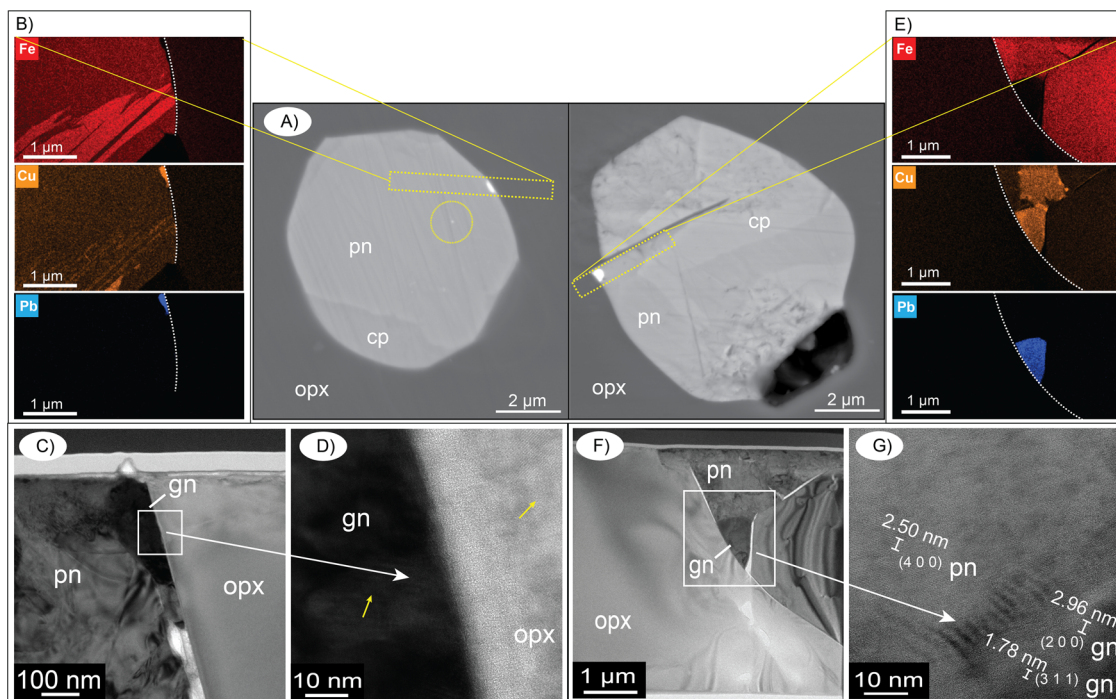


Fig. 3 Sulfide-hosted galena nanoinclusions in Fortuna lamproite dykes. Backscatter electron images of nanoparticle-bearing sulfide droplets acquired at scanning electron microscope on polished thin sections of Fortuna lamproite dykes (A). EDS elemental maps (Fe, Cu, Pb) on thin-foil focused-ion beam (FIB) samples analyzed by transmission electron microscopy (TEM) (B, E). Bright-field images in scanning transmission electron microscopy (STEM mode; C, F) and high-resolution TEM images (D, G) of the contact between the galena nanoinclusions and the adjacent minerals. Estimated measurements (nm) of ten spacings and corresponding lattice parameters are shown for each mineral domain. Mineral abbreviations are opx orthopyroxene; gn galena, pn pentlandite, and cp chalcopyrite.

Fortuna lamproite magmas, generated by partial melting of the underlying subduction-metasomatized SCLM^{38–40}, mechanically entrained Ni-Fe-Cu molten sulfides from the mantle source (represented by the Tallante xenoliths), and physically transported them as immiscible droplets to the overlying crust^{46,47} (Fig. 4). The presence of sulfide droplets as clinopyroxene-hosted inclusions in fusible domains of the SCLM¹¹ likely favored the mechanical removal of sulfide liquid during partial melting events in the mantle⁴⁸. Because sulfide liquids are denser ($\sim 4500 \text{ kg/m}^3$)⁴⁹ compared with silicate magmas ($\sim 2460\text{--}2710 \text{ kg/m}^3$ for lamproitic magmas)⁵⁰, the upwards transport of sulfide droplets necessarily requires that the sinking velocity of sulfide liquid is lower than the ascent velocity of the host lamproite magma. The ascent rates of silicate magmas rising through the continental lithosphere vary between 100–1000 m/yr for primitive basalts in arc settings^{51,52} to 4–50 m/s for kimberlites and similar volatile-rich magmas^{53,54} (Supplementary Note 2). On the other hand, the sinking velocity of sulfide droplets can be calculated according to Stokes' law for spherical bodies⁵⁵:

$$v = \frac{(\Delta\rho)}{18 * \mu} * g * d^2$$

using the density difference between sulfide and silicate melts ($\Delta\rho$), the diameter of the sulfide melt droplets ($d \sim 30 \mu\text{m}$ maximum), and the temperature-dependent viscosity (μ) of the silicate melt⁵⁶ (Supplementary Note 2). The calculated sinking velocities of sulfide droplets range from ~ 4 to 18 m/yr between 700–1200 °C (Table 2), which are orders of magnitude below the range of ascent rates expected for the lamproite magmas. Therefore, these calculations support that the Fortuna lamproite magmas may have efficiently scavenged the sulfide droplets from the SCLM during mantle melting, and transported them upwards across the whole mantle-to-crust magma route (Fig. 4). This transport mechanism is

especially effective through high-strain domains of the continental lithosphere⁴⁸, such as the trans-lithospheric fault zones that provided the locus of lamproite volcanism in southeast Spain⁴⁴. Moreover, the close textural association of sulfide droplets with fluid inclusions in the Fortuna lamproites provides evidence for the formation of buoyant compounds^{57,58} that possibly boosted the rapid upwards flux of dense sulfide liquid within ascending silicate magmas^{12,13}.

The sulfide droplets entrained in the lamproite magmas are expected to have concentrated the budget of chalcophile elements by chemical equilibrium partitioning with the host magmas¹⁷. Nevertheless, the occurrence of sulfide-hosted galena nanoinclusions, as well as native gold and Pt-(Pd)-Sn compounds in both the Tallante peridotite xenoliths and Fortuna lamproite dykes^{11,23,45}, suggests that these metals did not dissolve in the Ni-Fe-Cu sulfide liquid according to the expected chalcophile behavior. In particular, it is relevant to note that sulfide droplets in the Tallante xenoliths have Pb concentrations ranging between 1.58–280 ppm (Supplementary Data 1)¹¹, which are greatly below those required for attaining galena-saturation in the sulfide liquid ($\sim 60 \text{ wt}\%$ Pb⁵⁹). Moreover, despite galena having high melting temperatures around 1115 °C, experimental work predicts that PbS should fully dissolve in the Fe-Ni-Cu sulfide liquid at the high temperatures typical of mantle-derived magmas ($>850 \text{ °C}$)⁵⁹. According to these observations, galena nanoinclusions in mantle sulfides should be interpreted to have formed during the subsolidus re-equilibration of the sulfide assemblage exsolving at low temperatures. However, the galena nanoinclusion in the Tallante mantle xenolith displays a euhedral texture that, together with the lack of crystallographic continuity with the surrounding pentlandite matrix, argues against an origin by alteration or low-temperature exsolution of PbS previously dissolved in a homogeneous sulfide solution^{60,61}. Moreover, this galena nanoinclusion

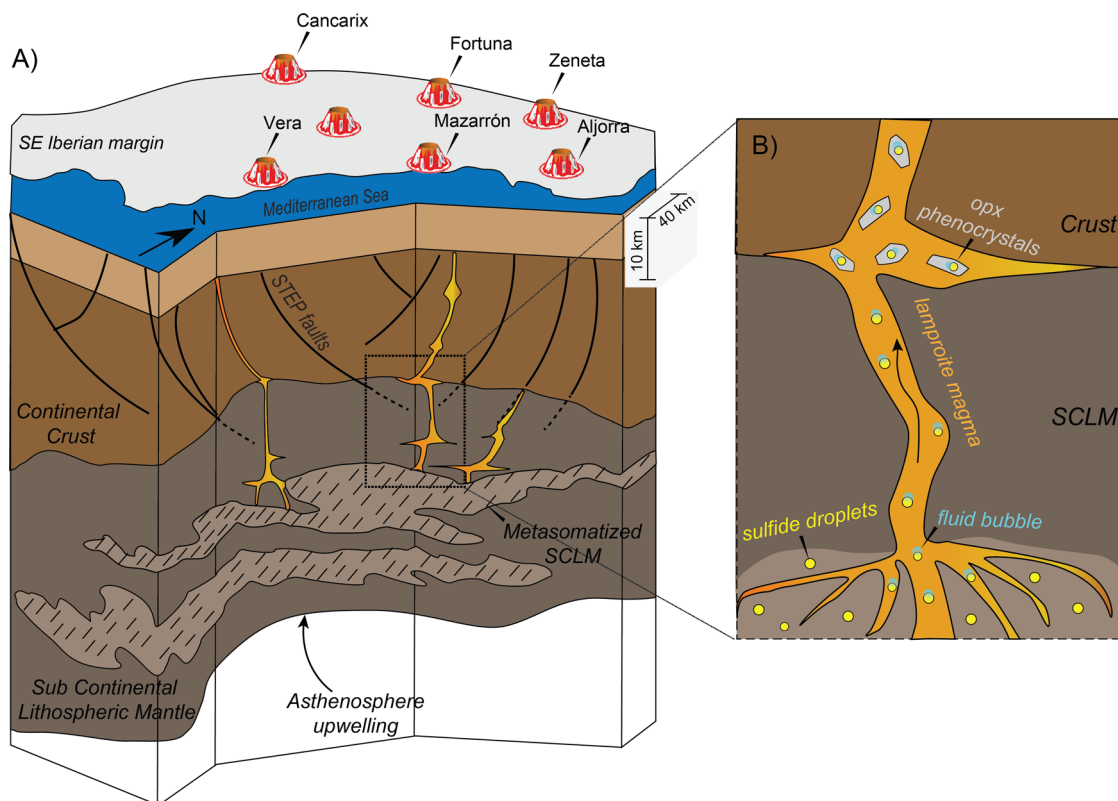


Fig. 4 Schematic transport model for metal flux through the continental lithosphere. A Cross-section sketch of the ore-productive continental lithosphere beneath the Neogene Volcanic Province of southeast Spain, modified after⁴⁴. STEP faults subduction transform edge propagator fault systems. **B** Model showing the physical transport of sulfide droplets in lamproite magmas ascending from the mantle source to the overlying crust.

Table 2 Calculated settling velocities of immiscible droplets of sulfide melt in lamproite magmas, based on relative density contrast ($\rho_{\text{sulfide}} - \rho_{\text{lamproite}}$), diameter of sulfide droplets (d), and temperature-dependent viscosities of the lamproite magmas (μ).

Settling velocities of sulfide melt droplets						
	$\rho_{\text{sulfide}} = 4500 \text{ kg/m}^3$		$\rho_{\text{lamproite}} = 2585 \text{ kg/m}^3$		$d = 30 \mu\text{m}$	
T [°C]	700	800	900	1000	1100	1200
μ [Kg/ms]	6.16	4.79	3.73	2.89	2.20	1.63
v [m/yr]	4.80	6.17	7.92	10.22	13.40	18.07
Ascent rate of silicate magmas						
v [m/yr]	arc basalts				100–1000	
v [m/day]	andesites				50–1000	
v [m/s]	volatile-rich magmas				4–50	

Ascent rates of silicate magmas are provided by refs. 51–54. Additional discussion on the calculation of settling velocities and magma ascent rates is provided in Supplementary Note 2.

is closely associated with a magnetite crystal (Supplementary Fig. 6), which was interpreted to have precipitated by the oxygen-rich fraction unmixing out of an oxysulfide melt due to local increase in fO_2 conditions^{23,62,63}. This spatial proximity rules out that the galena nanoinclusion crystallized by decreasing sulfur fugacity into reducing domains of the subarc lithospheric mantle, as proposed by ref. 64.

Rather, the well-defined crystal shapes and polygonal grain boundaries (Fig. 2A–C), coupled with the distinct lattice orientation relative to the host pentlandite (Fig. 2D), support the hypothesis that the galena nanoinclusion in the Tallante xenolith crystallized prior to the solidification of the host sulfide droplet. The EDS spectra and elemental mapping indicate that the galena nanoinclusion accommodated minor amounts of Cu into its crystal lattice⁴², thus potentially providing a mineralogical sink

also for other trace metalloids (e.g., Ag, Bi, and Sb)^{41,65}. The high-temperature crystallization of galena in a sulfide liquid having Pb concentrations largely below its solubility limit necessarily required the existence of a Pb–(Cu) nanomelt (blue star in Fig. 5), which was immiscible in the Ni–Fe sulfide liquid that precipitated the host sulfide (red star in Fig. 5). Immiscibility between Ni–Fe sulfide liquid and melts enriched in semi-metals (e.g., TABS: Te, As, Bi, and Se) has been experimentally demonstrated^{33,66}, but it has never been reported for Pb-bearing liquids in nature. This hypothesis is supported by the occurrence of galena nanoinclusion coexisting with a subspherical digenite halo along the edge surface of the sulfide droplet in the Tallante xenolith. According to experimental data, the co-existence of galena and digenite in crystallographic continuity (Fig. 2E–G) is consistent with the monotectic reaction below ~ 500 °C involving the solidification

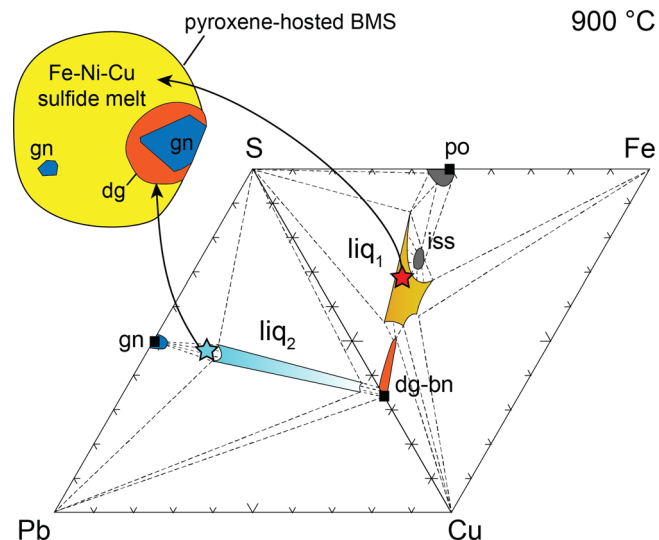


Fig. 5 Experimentally-determined phase relations at 900 °C in the Pb-Cu-S^{67,68} and Fe-Cu-S systems⁷⁵ applied for interpreting the origin of galena nano-inclusions in sulfide droplets from Tallante peridotites and Fortuna lamproites. Blue and red stars refer to the composition of the Pb-Cu nanomelt and the host sulfide liquid droplet, respectively.

of galena + digenite from a Pb-Cu-rich liquid plotting in the central portion of the Pb-Cu-S system^{42,67,68} (blue field in Fig. 5). Therefore, the attainment of the galena-digenite eutectic point necessarily required the existence of a pre-existing Pb(-Cu) nanomelt that was originally immiscible within the Ni-Fe sulfide liquid at high temperature (Fig. 5). Depending on the relative abundances of Cu and Pb, the immiscible nanomelt may have fully crystallized at high temperature as galena solid solution^{41,65} (Fig. 2B), or precipitated at low temperature (<500 °C) as galena + digenite upon xenolith ascent (Fig. 2E).

An analogous interpretation explains the origin of galena nanoparticles in the Fortuna lamproites, which likewise display curvilinear morphologies adapting to the rounded surface of the host sulfide droplet (Fig. 3). The lack of any orientation relationships relative to the pentlandite-chalcopyrite intergrowths (Fig. 3B), together with the rounded morphologies at the edge surface of the sulfide droplet (Fig. 3C, E, F), support the hypothesis that the galena nanoparticles crystallized from a Pb(-Cu) nanomelt that was immiscible within the Ni-Fe sulfide liquid that precipitated their host sulfide. These observations reinforce the idea that metal transfer across the ore-productive continental lithosphere of the southeastern Iberian margin occurred through the entrapment of metal-rich nanomelts within sulfide liquid droplets, which were transported upwards by lamproitic magmas ascending through the continental lithosphere. This transport mechanism explains why similar parageneses of metal-rich nano-inclusions, such as galena and native gold, are hosted in both the mantle source (sampled by the Tallante peridotite xenolith)¹¹ and the corresponding magmatic outputs (the Fortuna lamproite dykes)⁴⁵.

These observations provide the first-ever direct geological record of the experimental predictions that metal-rich nanoparticles, such as those commonly reported in base-metal sulfides worldwide^{11,23,26,60,61}, may precipitate from pre-existing small droplets of nanomelts that were originally immiscible within sulfide liquids even at concentrations that are below their solubility limit^{32,33}. Therefore, we argue that the close association of metal-rich nanoparticles with magmatic sulfides may be in part due to mechanical entrapment mechanisms, rather than solely to chalcophile equilibrium partitioning^{30,31}. Sulfide liquids may act as a physical trap collecting through preferential coalescence or

agglomeration the inventory of metal-rich immiscible nanomelts that were already present in the silicate magmas³³, thus potentially inheriting pre-existing metallic anomalies of the host silicate magmas that were generated by deeper melting processes, rather than during magmatic differentiation^{22,24,26}. According to this model, the metal enrichment of mantle-derived sulfide droplets is regulated by the amount of metal-rich nanomelts that they could have collected mechanically during magma ascent.

To test this hypothesis, we inspected the time-resolved spectra of the laser ablation analysis of sulfide droplets in the Tallante mantle xenoliths (Supplementary Data 1)¹¹. We found out that 43 out of 66 spectra have sharp spikes in the Pb signals that are likely associated with the presence of galena nano-inclusions in the sulfide. It is relevant to note that sulfide droplets lacking Pb spikes in their time resolve spectra display a narrow range of Pb concentrations (~14.4–48.7 ppm), whereas sulfide droplets bearing galena nano-inclusions exhibit much more scattered Pb abundances spanning from 1.58 to 280 ppm (Supplementary Data 1)¹¹. These values are consistent with the Pb concentrations calculated by mass balance for a sulfide droplet of ~20 μm diameter containing one 100 nm, or 1 μm sized galena nano-inclusion (Pb = 2.16 up to 216 ppm), respectively (Supplementary Data 1). Furthermore, we found out that 25 out of 66 time resolve spectra also have sharp spikes in the Au signals (Supplementary Data 1), which likely reflect the presence of native gold nano-inclusions in the Tallante sulfide droplets¹¹. Notably, sulfide droplets hosting such native gold nano-inclusions exhibit Au concentrations up to 46 ppm, which are greatly above the values reported for sulfide droplets lacking Au spikes in their time resolve spectra (~0.11–1.20 ppm; Supplementary Data 1). These values are consistent with Au concentrations expected by mass balance for a 20 μm sized sulfide droplet incorporating one 0.5 μm sized inclusion of native gold (62.5 ppm, Supplementary Data 1). Therefore, these observations suggest that the mechanical incorporation of metal-rich nanomelts and/or nanoparticles provides a previously unreported, feasible pathway for boosting the metal content of sulfide droplets that are fluxed by silicate magmas ascending through the continental lithosphere.

These findings highlight the necessity to revise the reliability of traditional models of metal transport based solely on sulfide solubility and sulfide/silicate equilibrium partitioning, and require considering transport as nanomelts governed by surface energy properties^{30,31}. In fact, the mechanical transfer of metal-rich nanomelts may potentially upgrade the metal budgets of sulfide liquids that eventually precipitate magmatic ores, beyond values predicted by chemical partitioning and hypothetical volume ratios with the host silicate magmas (R-factor). These mechanisms could provide a critical factor for focusing the deposition of large amounts of metals in magmatic sulfide deposits without requiring huge volumes of silicate magmas to equilibrate with^{69,70}. Furthermore, the preferential nucleation and/or agglomeration of fluid bubbles close to sulfide liquid droplets¹² may enhance the transfer of metal-rich nanomelts from dissolving sulfides into the hydrothermal fluids that exsolve from silicate magmas at shallow crustal depths¹³. The magmatic-hydrothermal transit of nanomelts may thus operate as a key process for sourcing colloidal metal-rich nanoparticles^{14,27–29,71} that are distributed by mineralizing fluids at various crustal levels. In this regard, the preservation of mantle-derived isotopic compositions in hydrothermal ore mineralizations may underpin the persistence of immiscible nanomelts throughout the whole mantle-to-crust metal transport network^{9,72,73}.

Methods

Scanning electron microscopy. Metal-rich nano-inclusions were detected by preliminary scanning electron microscopy on polished thin sections. These analyses were performed by using a QEMSCAN 650 F field emission gun-environmental scanning electron microscope (FEG-ESEM) equipped with energy

dispersive X-ray spectroscopy (EDS), secondary electrons (SE), and backscattered electrons (BSE) detectors at the Centro de Instrumentación Científica (CIC), Universidad de Granada (Spain). Operating conditions were 20 kV accelerating voltage for a 5 µm spot-size, and the intensity of beam current was optimized to a sufficient number of counts during EDS microanalysis.

Thin-foil sampling. Electron transparent thin (~90 nm) foil samples were prepared and extracted from selected nanoparticle-bearing sulfides by using a focused-ion beam scanning electron microscope (FIB-SEM) in the Laboratorio de Microscopías Avanzadas (LMA) at the Instituto de Nanociencia de Aragón (INA), Universidad de Zaragoza (Spain). Thin-foil sampling was performed with a Dual Beam FEI-Thermo Fisher Scientific, model Helios 650. The selected regions of interest were firstly covered with a ~300 nm carbon strip by focused electron beam-induced deposition and, subsequently, with a ~1 µm platinum strip in order to protect the thin foils from physical damage during ion milling, polishing, and extraction processes. The bulk material was removed on both sides of the lamellae by a rough Ga⁺ ion milling with a 30 kV current at 2.5 nA. The lamellae were then polished with a 30 kV current at 0.23 A and transferred to a TEM grid using an OmniProbe nanomanipulator with a tungsten tip. Ion-beam-assisted Pt deposition was performed in order to weld the lamellae to the TEM grid. Electron transparency of the thin foil samples was achieved by milling the lamellae with a 5 kV current at 68 pA and monitored with an Everhart-Thornley secondary electrons detector.

High-resolution transmission electron microscopy. The thin foil samples were analyzed by using an FEI Titan G2 transmission electron microscope (TEM) equipped with field emission gun cannon XFEG at the CIC facilities of the Universidad de Granada (Spain). This microscope is equipped with spherical correction for the objective lens, four detectors of X-rays energy dispersion (EDX) (FEI microanalysis Super X), and a high angle-annular dark field detector (HAADF). High-magnification electron microscopy images (HMEM) and high-resolution transmission electron images (HR-TEM) were acquired using a Gatan CCD Camera. The instrument was operated at 300 kV accelerating voltage. The textural and chemical characterization of selected areas of interest was carried out by a combination of EDX elemental maps, HAADF Z-contrast, and bright-field scanning transmission electron (STEM) imaging, coupled with HR-TEM imaging down to the atomic scale. The obtained images were subsequently processed with Digital Micrograph® Version 1.71.38, and maps with INCA® Microanalysis Suite version 4.09 software package. Structural data of minerals were obtained by selected area electron diffraction patterns (SAED) and/or by single-crystal fast Fourier transforms (FFT) calculated from HR-TEM images.

Data availability

The data generated in this study are available at <https://doi.org/10.6084/m9.figshare.23599818.v1>.

Received: 10 January 2023; Accepted: 3 July 2023;

Published online: 14 July 2023

References

- Vidal, O., Goffé, B. & Arndt, N. Metals for a low-carbon society. *Nat. Geosci.* **6**, 894–896 (2013).
- Hronsky, J., Groves, D. I., Loucks, R. R. & Begg, G. C. A unified model for gold mineralisation in accretionary orogens and implications for regional-scale exploration targeting methods. *Miner. Depos.* **47**, 339–358 (2012).
- Barnes, S. J., Cruden, A. R., Arndt, N. & Saumur, B. M. The mineral system approach applied to magmatic Ni–Cu–PGE sulphide deposits. *Ore Geol. Rev.* **76**, 296–316 (2016).
- Begg, G. C. et al. The lithospheric architecture of Africa: Seismic tomography, mantle petrology, and tectonic evolution. *Geosphere* **5**, 23–50 (2009).
- Wiemer, D. et al. Ancient structural inheritance explains gold deposit clustering in northern Perú. *Geology* **50**, 1197–1201 (2022).
- Schettino, E. et al. A fragment of inherited Archaean lithospheric mantle rules the metallogeny of central Mexico. *Int. Geol. Rev.* 1–25 (2022).
- Griffin, W. L., Begg, G. C. & O'Reilly, S. Y. Continental-root control on the genesis of magmatic ore deposits. *Nat. Geosci.* **6**, 905–910 (2013).
- Tassara, S. et al. Plume-subduction interaction forms large auriferous provinces. *Nat. Commun.* **8**, 1–7 (2017).
- Tassara, S. et al. Osmium isotopes fingerprint mantle controls on the genesis of an epithermal gold province. *Geology* **50**, 1291–1295 (2022).
- Holwell, D. A. et al. A metasomatized lithospheric mantle control on the metallogenic signature of post-subduction magmatism. *Nat. Commun.* **10**, 1–10 (2019).
- Schettino, E. et al. Metallogenic fingerprint of a metasomatized lithospheric mantle feeding gold endowment in the western Mediterranean basin. *Geol. Soc. Am. Bull.* **134**, 1468–1484 (2022).
- Blanks, D. E. et al. Fluxing of mantle carbon as a physical agent for metallogenic fertilization of the crust. *Nat. Commun.* **11**, 1–11 (2020).
- Heinrich, C. A. & Connolly, J. A. Physical transport of magmatic sulfides promotes copper enrichment in hydrothermal ore fluids. *Geology* **50**, 1101–1105 (2022).
- Petrella, L. et al. Nanoparticle suspensions from carbon-rich fluid make high-grade gold deposits. *Nat. Commun.* **13**, 1–9 (2022).
- Zelenski, M. et al. Silicate-sulfide liquid immiscibility in modern arc basalt (Tolbachik volcano, Kamchatka): Part I. Occurrence and compositions of sulfide melts. *Chem. Geol.* **478**, 102–111 (2018).
- Holwell, D. A. et al. Mobilisation of deep crustal sulfide melts as a first order control on upper lithospheric metallogeny. *Nat. Commun.* **13**, 1–12 (2022).
- Li, Y. & Audétat, A. Partitioning of V, Mn, Co, Ni, Cu, Zn, As, Mo, Ag, Sn, Sb, W, Au, Pb, and Bi between sulfide phases and hydrous basanite melt at upper mantle conditions. *Earth Planet. Sci. Lett.* **355**, 327–340 (2012).
- Core, D. P., Kesler, S. E. & Essene, E. J. Unusually Cu-rich magmas associated with giant porphyry copper deposits: evidence from Bingham, Utah. *Geology* **34**, 41–44 (2006).
- Loucks, R. R. & Mavrogenes, J. A. Gold solubility in supercritical hydrothermal brines measured in synthetic fluid inclusions. *Science* **284**, 2159–2163 (1999).
- Ulrich, T., Günther, D. & Heinrich, C. A. Gold concentrations of magmatic brines and the metal budget of porphyry copper deposits. *Nature* **399**, 676–679 (1999).
- Simmons, S. F. & Brown, K. L. Gold in magmatic hydrothermal solutions and the rapid formation of a giant ore deposit. *Science* **314**, 288–291 (2006).
- González-Jiménez, J. M. et al. Magmatic platinum nanoparticles in metasomatic silicate glasses and sulfides from Patagonian mantle xenoliths. *Contrib. to Mineral. Petrol.* **174**, 1–18 (2019).
- González-Jiménez, J. M. et al. Mineralogy of the HSE in the subcontinental lithospheric mantle—an interpretive review. *Lithos* **372**, 105681 (2020).
- Kamenetsky, V. S. et al. Crystallization of platinum-group minerals from silicate melts: Evidence from Cr-spinel-hosted inclusions in volcanic rocks. *Geology* **43**, 903–906 (2015).
- Zelenski, M. et al. Platinum-group elements and gold in sulfide melts from modern arc basalt (Tolbachik volcano, Kamchatka). *Lithos* **290**, 172–188 (2017).
- Kamenetsky, V. S. & Zelenski, M. Origin of noble-metal nuggets in sulfide-saturated arc magmas: A case study of olivine-hosted sulfide melt inclusions from the Tolbachik volcano (Kamchatka, Russia). *Geology* **48**, 620–624 (2020).
- Petrella, L. et al. Colloidal gold transport: a key to high-grade gold mineralization? *Miner. Depos.* **55**, 1247–1254 (2020).
- Hastie, E. C. G., Schindler, M., Kontak, D. J. & Lafrance, B. Transport and coarsening of gold nanoparticles in an orogenic deposit by dissolution–reprecipitation and Ostwald ripening. *Commun. Earth Environ.* **2**, 1–9 (2021).
- McLeish, D. F. et al. Colloidal transport and flocculation are the cause of the hyperenrichment of gold in nature. *Proc. Natl Acad. Sci. USA* **118**, 2100689118 (2021).
- Tredoux, M., Davies, G., McDonald, I. & Lindsay, N. M. The fractionation of platinum-group elements in magmatic systems, with the suggestion of a novel causal mechanism. *South Afr. J. Geol.* **98**, 157–167 (1995).
- Ballhaus, C. & Sylvester, P. Noble metal enrichment processes in the Merensky Reef, Bushveld Complex. *J. Petrol.* **41**, 545–561 (2000).
- Helmy, H. M. et al. Noble metal nanoclusters and nanoparticles precede mineral formation in magmatic sulphide melts. *Nat. Commun.* **4**, 1–7 (2013).
- Anenburg, M. & Mavrogenes, J. A. Noble metal nanonugget insolubility in geological sulfide liquids. *Geology* **48**, 939–943 (2020).
- Duggen, S., Hoernle, K., van den Bogaard, P. & Garbe-Schönberg, D. Post-collisional transition from subduction-to intraplate-type magmatism in the westernmost Mediterranean: evidence for continental-edge delamination of subcontinental lithosphere. *J. Petrol.* **46**, 1155–1201 (2005).
- Arribas, A. et al. Geology, geochronology, fluid inclusions, and isotope geochemistry of the Rodalquilar gold alunite deposit, Spain. *Econ. Geol.* **90**, 795–822 (1995).
- Milot, J. et al. Silver isotope and volatile trace element systematics in galena samples from the Iberian Peninsula and the quest for silver sources of Roman coinage. *Geology* **50**, 422–426 (2022).
- Pérez-Valera, L. A. et al. Age distribution of lamproites along the Socovos Fault (southern Spain) and lithospheric scale tearing. *Lithos* **180**, 252–263 (2013).
- Bianchini, G. et al. Metasedimentary and igneous xenoliths from Tallante (Betic Cordillera, Spain): Inferences on crust–mantle interactions and clues for post-collisional volcanism magma sources. *Lithos* **220**, 191–199 (2015).
- Avanzinelli, R. et al. Subduction-related hybridization of the lithospheric mantle revealed by trace element and Sr–Nd–Pb isotopic data in composite xenoliths from Tallante (Betic Cordillera, Spain). *Lithos* **352**, 105316 (2020).
- Casalini, M. et al. Petrogenesis of Mediterranean lamproites and associated rocks: The role of overprinted metasomatic events in the post-collisional lithospheric upper mantle. *Geol. Soc. Spec. Publ.* **513**, 271–296 (2021).

41. George, L., Cook, N. J., Ciobanu, C. L. & Wade, B. P. Trace and minor elements in galena: a reconnaissance LA-ICP-MS study. *Am. Mineral.* **100**, 548–569 (2015).
42. Johto, H. & Taskinen, P. Phase stabilities and thermodynamic assessment of the system Cu–Pb–S. *Miner. Eng.* **42**, 68–75 (2013).
43. Sharygin, V. V., Pospelova, L. N., Smirnov, S. Z. & Vladykin, N. V. Ni-rich sulfide inclusions in early lamproite minerals. *Russ. Geol. Geophys.* **44**, 855–866 (2003).
44. Cambeses, A. et al. Mineralogical evidence for lamproite magma mixing and storage at mantle depths: Socovos fault lamproites, SE Spain. *Lithos* **266**, 182–201 (2016).
45. Toscani, L. Magmatic gold grains in the El Tale lamproite, Fortuna, SE Spain. *Mineral. Mag.* **63**, 595–602 (1999).
46. Bockrath, C., Ballhaus, C. & Holzheid, A. Fractionation of the platinum-group elements during mantle melting. *Science* **305**, 1951–1953 (2004).
47. Ballhaus, C. et al. Fractionation of the noble metals by physical processes. *Contrib. Mineral. Petrol.* **152**, 667–684 (2006).
48. Wang, Z., Jin, Z., Mungall, J. E. & Xiao, X. Transport of coexisting Ni–Cu sulfide liquid and silicate melt in partially molten peridotite. *Earth Planet. Sci. Lett.* **536**, 116162 (2020).
49. Mungall, J. E. & Su, S. Interfacial tension between magmatic sulfide and silicate liquids: Constraints on kinetics of sulfide liquation and sulfide migration through silicate rocks. *Earth Planet. Sci. Lett.* **234**, 135–149 (2005).
50. Rao, N. C., Kamde, G. D., Kale, H. S. & Dongre, A. In *Indian Dykes: Geochemistry, Geophysics and Geochronology* (eds Srivastava, R. K., Sivaji, Ch. & Chalapathi Rao, N. V.) (Narosa Publishing House Pvt. Ltd., 2008).
51. Turner, S., Evans, P. & Hawkesworth, C. Ultrafast source-to-surface movement of melt at island arcs from ²²⁶Ra–²³⁰Th systematics. *Science* **292**, 1363–1366 (2001).
52. Turner, S. & Costa, F. Measuring timescales of magmatic evolution. *Elements* **3**, 267–272 (2007).
53. Sparks, R. S. J. et al. Dynamical constraints on kimberlite volcanism. *J. Volcanol. Geotherm. Res.* **155**, 18–48 (2006).
54. Wilson, L. & Head, J. W. An integrated model of kimberlite ascent and eruption. *Nature* **447**, 53–57 (2007).
55. Holzheid, A. Separation of sulfide melt droplets in sulfur saturated silicate liquids. *Chem. Geol.* **274**, 127–135 (2010).
56. Giordano, D., Russell, J. K. & Dingwell, D. B. Viscosity of magmatic liquids: a model. *Earth Planet. Sci. Lett.* **271**, 123–134 (2008).
57. Mungall, J. E. et al. Transport of metals and sulphur in magmas by flotation of sulphide melt on vapour bubbles. *Nat. Geosci.* **8**, 216–219 (2015).
58. Iacono-Marziano, G. et al. The critical role of magma degassing in sulphide melt mobility and metal enrichment. *Nat. Commun.* **13**, 1–10 (2022).
59. Brett, R. & Kullerud, G. The Fe–Pb–S system. *Econ. Geol.* **62**, 354–369 (1967).
60. Wirth, R., Reid, D. & Schreiber, A. Nanometer-sized platinum-group minerals (PGM) in base metal sulfides: New evidence for an orthomagmatic origin of the Merensky Reef PGE ore deposit, Bushveld Complex, South Africa. *Can. Mineral.* **51**, 143–155 (2013).
61. Junge, M. et al. Mineralogical siting of platinum-group elements in pentlandite from the Bushveld Complex, South Africa. *Miner. Depos.* **50**, 41–54 (2015).
62. Doyle, C. D. & Naldrett, A. J. The oxygen content of “sulfide” magma and its effect on the partitioning of nickel between coexisting olivine and molten ores. *Econ. Geol.* **82**, 208–211 (1987).
63. Laroque, A. C., Stimac, J. A., Keith, J. D. & Huminicki, M. A. Evidence for open-system behavior in immiscible Fe–S–O liquids in silicate magmas: implications for contributions of metals and sulfur to ore-forming fluids. *Can. Mineral.* **38**, 1233–1249 (2000).
64. Kepezhinskas, P., Berdnikov, N., Kepezhinskas, N. & Konovalova, N. Metals in Avachinsky peridotite xenoliths with implications for redox heterogeneity and metal enrichment in the Kamchatka mantle wedge. *Lithos* **412**, 106610 (2022).
65. Chutas, N. I., Kress, V. C., Ghiorso, M. S. & Sack, R. O. A solution model for high-temperature PbS–AgSb₂–AgBi₂ galena. *Am. Mineral.* **93**, 1630–1640 (2008).
66. Helmy, H. M. & Botcharnikov, R. Experimental determination of the phase relations of Pt and Pd antimonides and bismuthinides in the Fe–Ni–Cu sulfide systems between 1100 and 700° C. *Am. Mineral.* **105**, 344–352 (2020).
67. Shishin, D., Chen, J. & Jak, E. Thermodynamic modeling of the Pb–S and Cu–Pb–S systems with focus on lead refining conditions. *J. Phase Equilibria Diffus.* **41**, 218–233 (2020).
68. Craig, J. R. & Kullerud, G. Phase relations and mineral assemblages in the copper–lead–sulfur system. *Am. Mineral.* **53**, 145–161 (1968).
69. Holwell, D. A., Keays, R. R., McDonald, I. & Williams, M. R. Extreme enrichment of Se, Te, PGE and Au in Cu sulfide microdroplets: evidence from LA-ICP-MS analysis of sulfides in the Skaergaard Intrusion, east Greenland. *Contrib. Mineral. Petrol.* **170**, 1–26 (2015).
70. Fiorentini, M. L. et al. Post-collisional alkaline magmatism as gateway for metal and sulfur enrichment of the continental lower crust. *Geochim. Cosmochim. Acta* **223**, 175–197 (2018).
71. González-Jiménez, J. M. et al. Mechanisms for PdAu enrichment in porphyry-epithermal ores of the Elatsite deposit, Bulgaria. *J. Geochem. Explor.* **220**, 106664 (2021).
72. González-Jiménez, J. M. et al. Transfer of Os isotopic signatures from peridotite to chromitite in the subcontinental mantle: insights from in situ analysis of platinum-group and base-metal minerals (Ojén peridotite massif, southern Spain). *Lithos* **164**, 74–85 (2013).
73. Saintilan, N. J. et al. Osmium isotopic constraints on sulphide formation in the epithermal environment of magmatic-hydrothermal mineral deposits. *Chem. Geol.* **564**, 120053 (2021).
74. Gómez-Pugnaire, M. T., López Sánchez-Vizcaino, V., Fernández-Soler, J. M. & Acosta-Vigil, A. In *The Geology of Iberia: A Geodynamic Approach* (eds Quesada, C. & Oliveira, J. T.) Ch. 14 (Springer, 2019).
75. Kitakaze, A. Phase relation of some sulfide system-(4) especially Cu–Fe–S system. *Mem. Fac. Eng. Yamaguchi Univ.* **68**, 55–76 (2018).

Acknowledgements

This research was supported by the BES-2017-079949 Ph.D. fellowship to E.S. The Spanish projects PID2019-111715GB-I00/AEI/10.13039/501100011033, NANOMET PID2022-138768OB-I00, and MECOBE ProyExcel_00705 provided funding for field emission gun–environmental scanning electron microscopy (FEG-ESEM), focused-ion beam (FIB) and high-resolution transmission electron microscopy (HR-TEM). M.F. and F.P. acknowledge financial support from the Australian Research Council through ARC Linkage Project LP190100785. No permission was required to collect the samples during fieldwork. Research grants, infrastructures, and human resources leading to this research have benefited from funding from the European Social Fund and the European Regional Development Fund.

Author contributions

E.S., J.M.G.-J., and C.M. designed the study. E.S., J.M.G.-J., C.M., and M.F. were involved in extensive discussion and manuscript writing. F.P., I.F.B.-Q., F.G., R.B., and C.J.G. were involved in sampling. E.S. and F.P. performed optical microscope analysis, SEM imaging, and EDS mapping. E.S. and J.M.G.-J. performed FIB preparation and TEM analysis. All authors contributed to the interpretation of data and the manuscript text. Correspondence to Erwin Schettino.

Competing interests

The authors declare no competing interests.

Additional information


Supplementary information The online version contains supplementary material available at <https://doi.org/10.1038/s43247-023-00918-y>.

Correspondence and requests for materials should be addressed to Erwin Schettino.

Peer review information *Communications Earth & Environment* thanks Nicholas Barber and the other, anonymous, reviewer(s) for their contribution to the peer review of this work. Primary Handling Editors: Emma Nicholson and Joe Aslin. A peer review file is available.

Reprints and permission information is available at <http://www.nature.com/reprints>

Publisher's note Springer Nature remains neutral with regard to jurisdictional claims in published maps and institutional affiliations.

 **Open Access** This article is licensed under a Creative Commons Attribution 4.0 International License, which permits use, sharing, adaptation, distribution and reproduction in any medium or format, as long as you give appropriate credit to the original author(s) and the source, provide a link to the Creative Commons licence, and indicate if changes were made. The images or other third party material in this article are included in the article's Creative Commons licence, unless indicated otherwise in a credit line to the material. If material is not included in the article's Creative Commons licence and your intended use is not permitted by statutory regulation or exceeds the permitted use, you will need to obtain permission directly from the copyright holder. To view a copy of this licence, visit <http://creativecommons.org/licenses/by/4.0/>.

© The Author(s) 2023